A Systematic Study of Impurity Ion Poloidal Rotation and Temperature Profiles Using CXRS in the TJ-II Stellarator

Jose M. CARMONA, Kieran J. MCCARTHY, Victor TRIBALDOS and Maria A. OCHANDO

Laboratorio Nacional de Fusión, EURATOM-CIEMAT, E-28040 Madrid, Spain

A concise systematic study of impurity parameter profiles (impurity ion temperatures and poloidal velocities) measured under different plasma conditions has been carried out in the TJ-II stellarator using an active spectroscopic diagnostic system covering a large section of the central plasma minor radius, from $r/a = 0.3$ to 0.85, with high spatial resolution. For this, plasmas using hydrogen as the working gas were created and maintained using electron cyclotron resonance heating (from 400 to 500 kW) and line-averaged densities between 0.4 and 0.9×10^{19} m^{-3} were achieved. In the first instance, it is noted that ion temperature profiles tend to be flat across the accessible plasma radius, whilst a transition in the poloidal velocity from the ion to the electron diamagnetic direction is observed with increasing density. At the same time, the shear point for impurity velocity is seen to propagate outwards towards the plasma edge. Similarly, at a fixed density, a similar tendency is observed when raising the injected heating power. These results together with the behaviour of the impurity temperatures for the same conditions, suggest that collision frequency $\nu_E^{b/e} \sim n_e T_e^{-3/2}$ can be considered as an important control-parameter of plasma dynamics.

1. Introduction

Spatially resolved measurements of ion temperature and poloidal rotation are critical for understanding plasma dynamics. Indeed, these parameters are regularly measured in most medium and large fusion devices by means of spectroscopic and/or neutral particle analysis methods. Moreover, active techniques using accelerated neutral beams to stimulate spectral line and/or neutral particle emissions are now common [1, 2]. The advantage of active methods is that well-localized measurements can be obtained without the need to rely on inversion methods, which require knowledge of other parameters, or assumptions, with their inherent uncertainties. For spectroscopy this involves the capture of an electron, into an excited state, by a fully ionized impurity ion from the accelerated neutral beam. The decay by photon emission of the resultant ion provides a means of obtaining localized impurity temperatures (from Doppler line broadening) and velocities (from Doppler line shift) [1, 2]. Recently, such an active charge-exchange recombination spectroscopy (CXRS) diagnostic, based around a diagnostic neutral beam injector (DNBI) and a bidirectional (two vertical opposing views) multi-channel spectroscopic system [3, 4], began operation on the TJ-II, a four-period [5], low magnetic shear, stellarator. Moreover, when combined with a multi-channel fiber-optic based system profiles across the plasma minor radius can be obtained.

In this paper we begin by outlining the experimental set-up, system calibration methods and data analysis procedures used to achieve localized carbon ion temperature and poloidal velocity profiles. Next, we present results obtained from plasmas heated by electron cyclotron heated plasmas (ECRH) for different of conditions, e.g., when varying density or the injected ECRH. Finally, we discuss the results in light of the tendencies observed in parameter behaviour.

2. Experimental Details
2.1 Diagnostic set-up

The TJ-II is a four period heliac type stellarator ($B(0) \leq 1.2$ T, $R = 1.5$ m, $<a> \leq 0.22$ m) designed to explore a wide rotational transform range ($0.9 \leq \iota(0)/2\pi \leq 2.2$) in low, negative shear configurations ($\Delta\iota/\iota < 6\%$). The experiments reported here were carried out in electron cyclotron resonance heated (ECRH) plasmas ($P_{ECRH} = 300$ - 500 kW, 53.2 GHz, 2nd harmonic, X-mode polarization, $t_{discharge} \leq 250$ ms) with hydrogen as the working gas and with lithium-coated vacuum chamber walls [5] (previously boronized). No auxiliary NBI heating was provided. As a result, central electron densities and temperatures up to $\sim 10^{19}$ m^{-3} and ~ 1.5 keV respectively could be achieved. The strong reduction in impurity concentrations due to the wall-coating results in reduced impurity photon fluxes thereby requiring efficient detection procedures. For this, a high-throughput optical system and spectrograph, plus
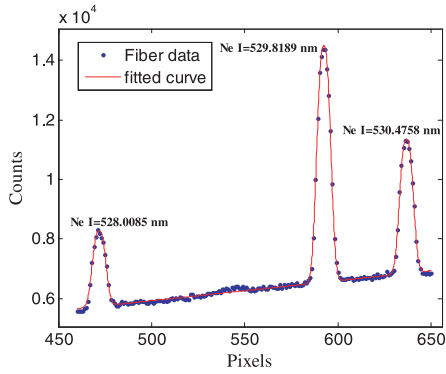
Fig. 1　Ne I lines used for calibration (close to 529 nm). Here, the x-axis is CCD pixel number. Neon wavelengths are taken from [8].

a high-efficiency detector made the goal of measuring in such conditions possible. These, together with the other system components, are described briefly below.

The DNBI, an upgraded version of the compact DINA-5 injector installed on the Madison Symmetric Torus device [6], provides 5 ms long pulses, up to two per discharge, of neutral hydrogen accelerated to 30 keV with an equivalent current of 3.3 equ. A. Its 1/e radius at focus is 21 mm. A bidirectional optical system, consisting of commercial camera lenses and fibre optic bundles designed to measure Doppler shifts and widths of the C VI line at λ = 529.06 nm in up 12 channels with ~1 cm spatial resolution across the plasma minor radius, was installed in top and bottom view ports located in the same machine sector as the DNBI. See Fig. 1 from Ref. [3]. The light dispersion element is a Holospec spectrograph with three 100 μm curved entrance slits (curved to compensate for the short focal length of the spectrograph) equipped with a transmission grating sandwiched between two BK7 prisms [7]. It provides a focal-plane dispersion of ~1.15 nm/mm at 529 nm. Moreover, a narrow bandpass filter (2.0 ± 0.5 nm at full-width at half-maximum, (FWHM)) prevents spectral overlapping of the light from the three fibre arrays at the image plane. The set-up also includes a high-efficiency back-illuminated CCD camera and a fast mechanical shutter (≥ 4.5 ms time window). With on-chip binning, multiple spectra can be collected during discharges (≤ 300 ms). Next, line-of-sight alignment was performed by illuminating each fibre bundle with a bright light source and observing, through a nearby viewport, the orientation and location of the resultant bright spots with respect to markings on the inside of the opposing vacuum flange. In this way, the sightlines through plasmas were determined using a cross-sectional machine drawing and magnetic configuration maps. Furthermore, by comparing with the neutral beam geometry, the normalized radius, r/a, corresponding to each beam/line-of-sight interaction volume was found. Finally, for the magnetic configuration used, 100-44-64, the viewing system covered the plasma minor radius from

r/a = 0.3 to 0.8. The radial spatial resolution achieved is almost constant across this range. However, towards both extremes the error bars on the measured parameters increase due to the reduced light collection in the optical system from these positions.

2.2　Instrument calibration

Calibration of individual fibres was performed in order to detect any small variations in the position and in the FWHM of spectral lines. Calibration spectra were captured between discharges using a retractile pencil-type Neon lamp positioned between the light collection lens and the fibre bundle head.

Wavelength calibration was performed using a second order (polynomial) fit to three nearby Ne I spectral lines (see Fig. 1). As spectra are recorded simultaneously for all fibres, fine corrections could be made for any nonlinear dispersion present in the spectrometer or displacement errors in the entrance slits. Next, the instrument function was determined from the same spectra using a Gaussian function fitting. This was found to be ~7.6 pixels (~1.14 Å) and ~6.3 pixels (~0.95 Å) for the central fibres of the top and bottom arrays respectively (Fig. 1 in [2]). It should be noted that the fits were made using a non-linear least squares method based on trust-region algorithms. For this, comparisons between different fitting methods were made (i.e., robust and non-robust). In general, robust algorithms are considered preferable to non-robust ones, as the former are less sensitive to outlier points (points numerically distant from the rest that can lead to misleading fits). However, here it was found that robust fits show significant fibre-to-fibre variations for both FWHMs and line centres whilst non-robust fits are more stable [9]. Indeed, in certain situations robust methods may be preferable, e.g., for single Gaussian fits, but they prove to be weak when multiple Gaussian fits are performed. Hence, the non-robust method was chosen as the fitting method.

2.3　Active and passive signal treatment

Special care must be taken when treating the CXRS line spectra. For instance, contributions to the measured signal from electron-excited emissions (called the *cold component* or *passive* signal, *P*) must be removed since these are not localized. Also, for the experimental set-up, plasma conditions should remain constant along a discharge, or discharges should be reproducible (shot to shot technique), so that the active signal, *A*, can be obtained by subtraction, i.e., (*A* + *P*) − *P* = *A*. See Fig. 2. For the data presented here, both techniques were employed.

2.4　Data analysis

The charge exchange process of interest here consists of the capture, by a fully-stripped carbon ion, C^{+6}, of an electron from a hydrogen atom of the neutral beam. The electron is captured into an upper-state of the resultant ion,

C^{+5}. De-excitation of the upper-state results in the emission of a photon, in this case, the emission of a 529.06 nm photon (1).

$$H^0 + C^{+6} \rightarrow H^+ + C^{+5}(n^*, l^*) \Rightarrow$$
$$\Rightarrow C^{+5}(n^*, l^*) \rightarrow C^{+5}(n, l) + h\nu \,(n^* > n). \tag{1}$$
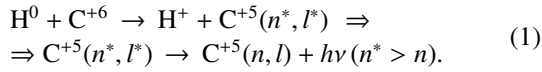
Such emissions provide information about C^{+6} ions via Doppler shifts and widths of the spectral line (temperatures and velocities respectively). Moreover, as the level lifetime of the upper C^{+5} level is $\sim 10^{-9}$ s, and the ions are predicted to rotate at $< 20\,\mathrm{km\,s^{-1}}$, emissions occur within the same localized volume as the charge exchange (i.e., well within 1 cm). Now the impurity ion temperatures and velocities are deduced from the usual relations:

$$T_{\mathrm{i}} = 1.68 \cdot 10^8 A \left(\frac{\Delta\lambda_{\mathrm{fwhm}}^2 - \Delta\lambda_{\mathrm{instrum}}^2}{\lambda_0^2} \right),$$
$$v = \left(\frac{\lambda - \lambda_0}{\lambda_0} \right) c, \tag{2}$$

where A is the mass of the ion [amu], $\Delta\lambda_{\mathrm{fwhm}}$ the measured FWHM, $\Delta\lambda_{\mathrm{instrum}}$ the instrument FWHM, λ and λ_0 are the measured and the unshifted central wavelength of line under consideration respectively and c the speed of light.

2.4.1 Additional corrections

A clear asymmetry was observed about the measured C VI spectral line. This was interpreted as arising from fine structures in the transitions in this hydrogen-like ion [4, 10]. Indeed, there can be up to 13 possible lines with different intensities depending on plasma conditions. Such fine structures give rise to the tail observed on the short wavelength side of the C VI spectral line (see Fig. 2) that results in excess line broadening, and hence overestimated ion temperatures. Thus, in order to correct for this a multi-Gaussian fit, using relative intensity ratios between fine structure components, was employed. In addition, after careful analysis, contamination by a nearby O VI line was ruled out, in particular as there is a strong oxygen reduction due to the coated walls.

3. Results

For the work undertaken here, hydrogen plasmas lasting up to 250 ms were created and line-averaged electron densities between 0.4 and $0.9 \times 10^{19}\,\mathrm{m^{-3}}$ were achieved. Moreover, CXRS data were obtained for plasmas created with different injected ECRH powers. Here, in the following sections, impurity temperature and rotation velocity profiles are presented for a variety of plasmas conditions. The tendencies observed in these parameters when changing plasma conditions are highlighted and discussed.

3.1 Temperature and poloidal velocity profiles

Impurity ion temperatures for two discharges with approximately 400 kW of ECRH, but different line averaged electron densities, $<n_{\mathrm{e}}>$, are plotted in Fig. 3. In the first instance, the values are in accordance with the weak collisional coupling for these densities. However, the impurity temperature is found here to be higher for the discharge with lower $<n_{\mathrm{e}}>$. It is also seen that temperature profiles are relatively flat except towards the edge (for $r/a \geq 0.7$) where these drop off. The impurity temperatures measured here for the higher density case are similar to those measured for majority ions using neutral particle analyser systems [11]. Moreover, the increased impurity temperature at low densities was seen previously using passive spectroscopy and accounted for by contributions due to non-thermal velocities [12].

Next, for the same set of discharges, poloidal rotation profiles are shown in Fig. 4. A clear transition from the ion to the electron diamagnetic direction is seen.

Moreover, for the lower line-averaged electron density, the ions rotate poloidally in the ion diamagnetic direction whereas for the higher density this rotation changes towards the electron diamagnetic direction. An in depth analysis of this change in rotation is performed for a detailed density scan. This is described below.
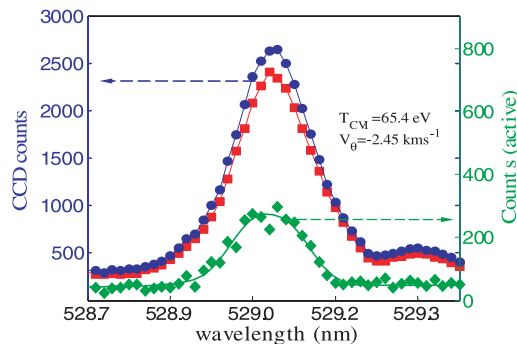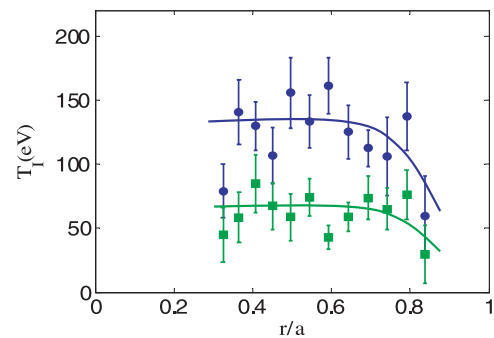

Fig. 2 C VI line spectra for consecutive CCD frames at $r/a = 0.55$. Diamonds, squares and dots represent active, passive and active+passive signals, respectively. A fit to the active C VI signal is shown.

Fig. 3 Ion temperature profiles obtained for two discharges with $P_{\mathrm{ECRH}} = 400$ kW and line averaged densities $<n_{\mathrm{e}}> = 0.42$ (dots) and 0.9 (squares) $\times 10^{19}\,\mathrm{m^{-3}}$. Lines are plotted to aid the reader.
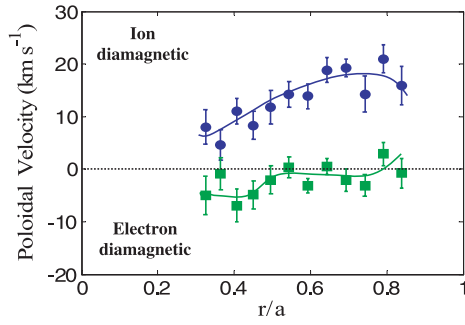
Fig. 4 Poloidal rotation profiles for the same discharges as shown in Fig. 3. The symbols used are the same as in Fig. 4. Lines are plotted to aid the reader.
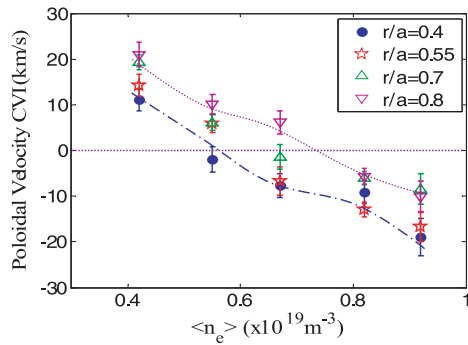

Fig. 5 A plot of impurity poloidal velocity as a function of line-averaged electron density showing the change from ion to electron diamagnetic direction. The symbols represent values at different normalized plasma radii, r/a.

3.2 Density scan

A density scan (from 0.4 to 0.92×10^{19} m^{-3}) with a fixed 400 kW of injected ECRH power was performed. The measured poloidal velocities are presented in Fig. 5. These show a change in direction, from ion to electron diamagnetic direction (transition from electron to ion root), as the line-averaged electron density is increased. A similar tendency was reported previously in the TJ-II for passive spectroscopy measurements of C V ion temperatures [13]. Here in Fig. 5, it is seen that the transition point (i.e., where the poloidal velocity ~ 0) gradually propagates towards the plasma edge (i.e., from $r/a \sim 0.4/0.55$ to $r/a \sim 0.7/0.8$) as $<n_e>$ increases, in this instance from ~ 0.55 to 0.8×10^{19} m^{-3}. These C^{+6} ion measurements provide the first experimental evidence that the shear point of the impurity ion rotation propagates outwards towards the plasma edge of TJ-II with increasing electron density. Moreover, by considering the basic equation that relates impurity rotation and the radial electric field,

$$V_{pol} = (E_r \times B)/B^2 - \text{grad } p_I \times B/n_I Z_I e B^2, \qquad (3)$$

where v_{pol} is the poloidal rotation velocity of the ion under investigation, p_I, n_I and Z_I are the pressure, density and charge of this ion respectively, e is electron charge, and E_r and B are the electric and magnetic fields respectively.
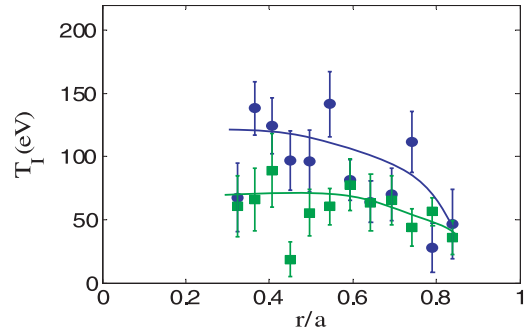

Fig. 6 C^{6+} ion temperature profiles for 400 kW (dots) and 500 kW (squares) of P_{ECRH} and almost the same line-averaged density $<n_e> = 0.6 \times 10^{19}$ m^{-3}.
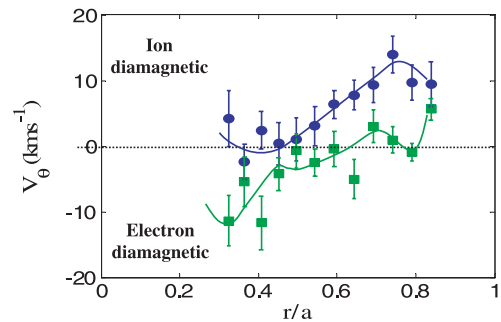

Fig. 7 C^{6+} ion rotation profiles for 400 kW (dots) and 500 kW (squares) of P_{ECRH}. Here the line-averaged electron density is about 0.6×10^{19} m^{-3}.

Here the first term is the familiar $E \times B$ drift while the second term represents the ion diamagnetic drift. It can be assumed for TJ-II that the toroidal rotation can be ignored, i.e., since $V_{pol} B_{tor} \gg V_{tor} B_{pol}$ due to the small B_{pol}/B_{tor} and the viscous damping between passing and trapped particles. In this case, since the change in sign of E_r is found to commence at the plasma edge and advance inwards as the density increases [14] it might indicate an important contribution of the impurity pressure gradient on this rotation.

3.3 P_{ECRH}

Impurity ion temperature and poloidal rotation profiles are compared for two different injected ECRH powers (400 kW and 500 kW) with comparable line-averaged electron densities. See Figs. 6 and 7.

Here, for fixed line-averaged density, the impurity temperature is seen to decrease with P_{ECRH}. In order to understand this it is necessary to consider the simple power balance equation given by

$$\frac{dT_b}{dt} = \nu_E^{b/e}(T_e - T_b) - \frac{T_b}{\tau_E^b}, \qquad (4)$$

where $\nu_E^{b/e} \sim n_e T_e^{-3/2}$, T_b and T_e are majority ion and electron temperatures respectively, and τ_E^b is majority ion confinement time. Here, better coupling (higher collision frequency $\nu_E^{b/e}$) between ion and electron species (increasing

$<n_e>$ or decreasing T_e) gives rise to increased ion temperature. Hence for a power scan (with fixed $<n_e>$ and non-constant T_e), or density scan (at fixed P_{ECRH}) the ion temperature can be expected to change, i.e., to increase when (i) T_e decreases (constant $<n_e>$) or (ii) $<n_e>$ increases. Moreover, the ion energy confinement time scales inversely with injected P_{ECRH} [15] thus enhancing the above point since (for fixed $<n_e>$) a lower injected P_{ECRH} implies higher ion temperatures. In ECRH discharges, ion and electron channels are strongly decoupled ($T_e \gg T_b$) as a consequence of the low electron densities and single channel heating. Thus for constant density, T_b should increase as T_e is decreased, i.e., lower P_{ECRH}, since T_e is an increasing function of P_{ECRH}.

Finally, for the same discharges as in the previous figure, the impurity rotation profile is seen to shift to the electron diamagnetic direction for the shot with higher P_{ECRH}. According to neoclassical theory, a shift to the ion diamagnetic direction could be in principle expected. As previously reported (see Fig. 7 of Ref. [13]), in TJ-II there is a transition from positive to negative radial electric field around a critical line-averaged density of 0.6×10^{19} m^{-3} and a region (see Fig. 3 of Ref. [13]) with three roots: a positive "electron" root, an unstable intermediate solution, and a negative "ion" root.

Unfortunately, the data currently available for the ECRH scan are precisely around this critical region. For the $P_{ECRH} = 400$ kW shot the density is slightly below ($<n_e> = 0.58 \times 10^{19}$ m^{-3}) this transition thereby indicating a positive E_r, whereas for $P_{ECRH} = 500$ kW, it is slightly above the critical density ($<n_e> = 0.61 \times 10^{19}$ m^{-3}) thus implying that the radial electric field is negative in accordance with the results of Ref. [13].

Note that the argument about power balance for the P_{ECRH} scan still holds, i.e., the ion temperature is determined by the power transferred by electrons via collisions and is lost through transport, in this simple modelling with an effective confinement time. For higher P_{ECRH} collisional coupling is reduced, and according to neoclassical theory, the confinement time is also reduced, because of the smaller radial electric field, both effects contributing in reducing the ion temperature as is found.

In conclusion, as seen from these experiments, dynamics depend on $<n_e>$ as well as on T_e (varied here by

P_{ECRH}). It is thus considered that the control-parameter is the plasma collision frequency $\nu_E^{b/e} \sim n_e T_e^{-3/2}$.

4. Summary

Radial profiles of impurity ion temperatures and poloidal velocities have been obtained for a range of plasma conditions in the TJ-II. A study of the behaviour of these parameters when changing density or injected ECRH power has been undertaken. Possible controlling mechanisms for the tendencies observed have been put forward. For instance, the tendencies observed in the impurity ion temperature profiles when varying either line-averaged density or injected P_{ECRH} (while maintaining the other parameter constant) suggest that the plasma collision frequency ($\sim n_e T_e^{-3/2}$) tends to control the dynamics in TJ-II, thereby providing a clearer description of the trigger mechanism.

With the impending coming on line of the second of TJ-II's two neutral beam injectors [16], as well as an Electron Bernstein Wave Heating system [17], the CXRS-DNBI diagnostic will be a powerful tool for the different heating scenario envisaged. Moreover, in the near future upgrades to the active diagnostic will be made in order to increase its scientific return.

[1] H. Ehmler *et al.*, Plasma Phys. Control. Fusion **45**, 53 (2003).
[2] S. Gangadhara *et al.*, Rev. Sci. Instrum. **77**, 10F109 (2006).
[3] R.C. Isler, Plasma Phys. Control. Fusion **36**, 171 (1994).
[4] K. Ida *et al.*, Rev. Sci. Instrum. **71**, 2360 (2000).
[5] E. Ascasíbar *et al.*, Fusion Eng. Des. **56-57**, 145 (2001).
[6] G.F. Abdrashitov *et al.*, Rev. Sci. Instrum. **72**, 34 (2001).
[7] R.E. Bell *et al.*, Rev. Sci. Instrum. **75**, 4158 (2004).
[8] A.S. Stringanov *et al,*. Tables of Spectral Lines of Neutral and Ionized Atoms, IFI/Plenum, New York, 1968.
[9] J.M. Carmona *et al.*, to be published.
[10] R.J. Fonck, Phys. Rev. A **29**, 3288 (1984).
[11] R. Balbín *et al.*, Proc.15th Inter. Stellarator Workshop, Madrid(2005), http://www-fusion.ciemat.es/SW2005/
[12] K.J. McCarthy *et al.*, Europhys. Lett. **63**, 49 (2003).
[13] B. Zurro *et al.*, Fusion Sci. Technol. **50**, 419 (2006).
[14] C. Hidalgo *et al.*, Phys. Rev. E **70**, 067402 (2004).
[15] R. Burhenn *et al.*, Fusion Sci. Technol. **46**,115 (2006).
[16] J. Guasp *et al.*, Fusion Technol. **35**, 32 (1999) .
[17] A. Fernández *et al.*, Fusion Sci. Technol. **46**, 335 (2004).